IAC-16,B1,2,8,x33950

A NOVEL APPROACH TO MICROWAVE INTERFEROMETRIC RADIOMETRY IN THE GEOSTATIONARY ORBIT USING FORMATION FLIGHT

Ahmed Kiyoshi Sugihara El Maghraby
University of Southampton, UK
asem1g14@southampton.ac.uk

Angelo Grubišić
University of Southampton, UK

Camilla Colombo
Politecnico di Milano, Italy

Adrian Tatnall
University of Southampton, UK

***Abstract*—A novel technique for Earth-observation microwave interferometric radiometry using satellite formation flight is presented. The concept allows large apertures of unprecedented sizes to be synthesised by means of antennas mounted on several free-flying platforms performing interferometry. The size of the synthesised aperture is determined by the furthest distance between the free-flying satellites. The concept is applicable to wide range of microwave frequencies, meaning that the large aperture may be applied to achieve unprecedented spatial resolution, to extend Earth observation radiometry to unprecedented long wavelengths, or to enable radiometry in the geostationary orbit. Two such concepts are presented, and as an example they are applied to geostationary radiometry at 10 GHz. The first concept employs a rotating Y-shaped interferometric radiometer in formation with a constellation of nine free-flying microsatellites. The effective diameter of the synthesised aperture is 14.4m, which produces a spatial resolution of 79.5 km at 10 GHz from the geostationary orbit. The total mass of the constellation can be within 2 tonnes, which may be deployed on a single launch vehicle. The second concept is a constellation of six formation-flying radiometers, which produce apertures of 28.8m, and produces a spatial resolution of 39.8 km at 10 GHz. While this configuration is capable of producing larger effective apertures, the total mass can exceed 5 tonnes, and may require multiple launches and rendezvous at the operational orbit. Both of these concepts can be scaled up for larger apertures, and are bound primarily by the number of satellites deployable in the constellation. The free-flying nature of the concept means they are susceptible to interferometric performance degradation by array deformation. The effect of deviation on the radiometric resolution is explored and found, concluding that deviation as small as 0.1λ can lead to performance degradation of up to 20 K. Annual ΔV required to maintain such constellations are also found at up to 2.23 m/s annually.**

I. INTRODUCTION

Passive microwave radiometry has been a highly fruitful area of satellite remote-sensing of the Earth, producing a wide variety of data products of both the ground and the atmosphere. To mention a few examples, the GPM Microwave Imager on board the Global Precipitation Mission produces vertical profiles for the atmosphere for humidity, snow and rain precipitation rates, and the Microwave Interferometric Radiometry using Aperture Synthesis on board Soil Moisture and Ocean Salinity measures global ocean salinity and soil moisture. Many such applications would benefit greatly from global, continuous and high temporal resolution measurement, that may be achieved from the geostationary orbit. One such area is in atmospheric profiling for temperature, humidity and liquid water content for Numerical Weather Prediction.

Currently all microwave radiometers are bound to the low Earth orbit due to the poor spatial resolution of microwave instruments. The temporal resolution as a result is limited by the revisit period, which is typically several days in the low orbits. The diffraction limit sets the spatial resolving power of an instrument, and is often quantified by the ratio λ/D, which is the ratio between the signal's wavelength and the diameter of an aperture. A typical optical instrument is in the order of 1×10^{-6}, while a typical microwave instrument is in the order of 1×10^{-3}. Such spatial resolution is absolutely inadequate for use in any orbit higher than low Earth orbits, and consequently all geostationary instruments to date for Earth observation are optical and IR instruments.

In the pursuit to achieve the aperture sizes required for geostationary radiometry, several mission concepts using interferometric techniques are now being explored, including the Geostationary Synthetic Thinned Aperture Radiometer (NASA), the Geostationary Atmospheric Sounder (ESA) and the Geostationary Interferometric Microwave Sounder (NSSC, China). [1], [2], [3] Aperture sizes achievable by these concepts are still bound by the size of a single satellite.

In this literature the concept of performing passive microwave interferometry using a fleet of formation-flying satellites is proposed. The achievable aperture sizes for such a concept, and hence the achievable spatial resolution, is bound by the number of satellites deployable in the constellation. As it is found in Section III, a single launch can already achieve apertures of unprecedented sizes. If need be, multiple launches may be used to further improve the spatial resolution of the instrument.

Although the primary focus of this study is the application of formation flight to enable microwave radiometry from the geostationary orbit, the concept is not limited to meteorological application, or indeed the geostationary orbit.

II. Multi-Satellite Interferometry

Interferometry, also known as aperture synthesis, is a branch of radiometry where instead of using mechanical steering to locate the radiating sources, signal phase differences between a distribution of numerous phase-sensitive antennas are measured to map the scene brightness temperature. This rids the interferometer the need for any mechanically moving parts, ultimately leading to larger antennas being deployable. Having been originally been developed for radio astronomy in the 1980's, the technique is mature, and it has recently been adapted for Earth observation by the Soil Moisture and Ocean Salinity (SMOS) mission, by its primary payload Microwave Interferometric Radiometry by Aperture Synthesis (MIRAS) in 2009.

In order to understand the relevance of formation flight to such a technique, it is important to note that interferometers do not directly measure the brightness temperature map. They instead measure an intermediate quantity called visibility, from which the brightness temperature map can be retrieved by post-processing on the ground.

The general relation between the visibility and the brightness temperature map is found as [9]

$$V = \iint^{\xi^2+\eta^2<1} \tilde{T}_B \hat{r} e^{-2\pi i(u\xi+v\eta+w\sqrt{1-\xi^2-\eta^2})} \mathrm{d}\xi \mathrm{d}\eta \quad (1)$$

where $V(u,v,w)$ is the visibility at baseline u,v,w, $\tilde{T}_B(\xi,\eta)$ is the modified brightness temperature at direction (ξ,η) and $\hat{r}$ is the fringe-washing function.

An intuitive interpretation of the visibility is possible with a planar array ($w = 0$) and negligible fringe-washing function ($\hat{r} = 1$). Under such conditions the visibility becomes the spatial Fourier transform of the modified brightness temperature map.

The interferometer measures the visibility in point-samples by taking the cross-correlation of the signals detected from every possible pair of antennas, called baseline pairs. Each baseline pair is separated by the baseline vector $[u,v,w]\lambda$ where u, v and w are distance vector components in the x, y and z directions, normalised by the signal wavelength λ, and where z is parallel to the interferometer bore-sight. With a set of all possible baseline pairs, the visibility sample is taken.

The distribution of the point-samples taken of the visibility is called the visibility sampling pattern, and is the key determinant of the interferometer imaging performance. This pattern is unique to the distribution of the antennas, hence the design of this distribution is an important consideration in designing an interferometer. As an example, the array geometry of a Y-shaped array and its resultant visibility sampling pattern is shown in Figure 1. This is the configuration chosen for MIRAS, and is the most efficient. The vectors between all possible pairs of antennas are the baselines, and constitute the visibility sampling pattern.

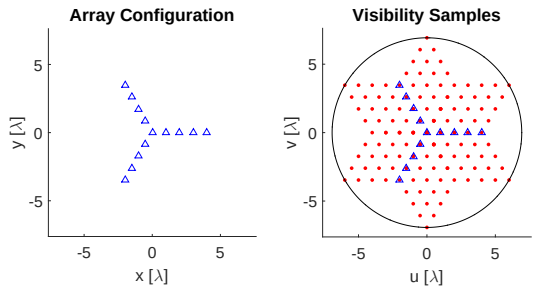

Fig. 1: An example of a Y-shaped interferometer with 4 antenna elements per arm, each separated by one wavelength (left). Right shows the resultant visibility sampling points in red. Overlain also is the array geometry, to show the relationship between the array and the samples. By rotating the array, all visibility within the circular bound can be sampled.

Because the visibility can be seen as the Fourier transform of the modified brightness temperature, visibility sampled further away from the origin represent higher spatial frequency component of the modified brightness temperature map, contributing to better spatial resolution. This means the spatial resolution of the interferometer is determined by the distance between the two furthest apart antennas.

This also means that in order for the spatial resolution to be equal in all directions, and for a clean beam, the visibility sample should ideally be circular. [4] One of the recent innovation is to rotate the interferometer in order to achieve this circular visibility sample. [2], [3] Shown in Figure 1 is a circular area bound by the longest baseline, within which the visibility is sampled by rotating the array by 60 degrees.

This study combines the benefits of the rotating interferometer with the benefits of multiple formation-flying interferometers. Two approaches are explored of this concept. The first case explores the effect of introducing a single antenna element to the rotating interferometer. The second case explores the effect of introducing an identical copy of the first array. The consequences of these two cases on the visibility sampling pattern are now explored.

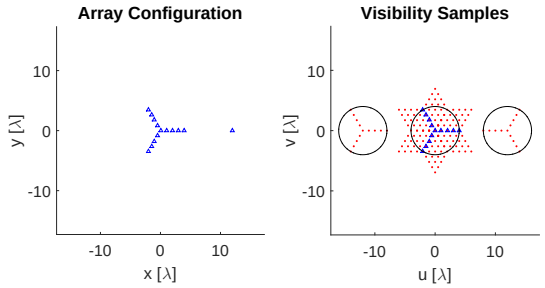

Fig. 2: Effect of introducing a single element to an array.

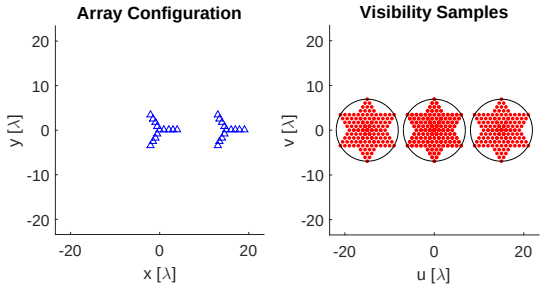

Fig. 3: Effect of introducing a duplicate of an array.

A. *Single-Element Companions*

Given an array of antennas, the effect of introducing a single element some distance away to the array is that the geometry of the array appears in the visibility sample. This is shown in Figure 2, where in addition to the visibility sample of the main array, the geometry of the array the central array is introduced at $(u, v) = (12\lambda, 0)$. This location reflects exactly the location of the single element, and is an important design parameter.

Furthermore, by rotating the central array while maintaining the single element at a constant location, each of the visibility samples rotate about their respective centres. This becomes useful when only considering the visibility samples taken between the arms and the element located at the root of the arms (shown in blue in Figure 2) and between the arms and the single elements. This introduces symmetry to the sampling pattern, and enables the constellation to be scaled up as it is shown in Section III).

B. *Array Duplication*

Given an array of antennas, the effect of placing an identical array some distance away is that a copy of the visibility sampling pattern of the individual array is produced at the location of the second array.

An example of this is shown in Figure 3, where a second Y-shaped array is placed at $(u, v) = (15\lambda, 0)$. The result is the second visibility sampling pattern appears at the location.

Similarly, by rotating both arrays at the same direction and rate, both sampling patterns rotate about their respective centres. In this case, symmetry already exists between all sampling patterns, and all samples can be considered.

The observation of the effect of introducing single elements to an interferometer, and duplicating an array motivates the derivation of the two concepts. One, with a constellation of many, identical satellites, the arrays of which are rotating, and another, a constellation of a single large satellite with many companion microsatellites.

III. The Single-Element Companion Concept

As a direct development from Section II-A, a lattice of Single-Element Companions are placed such that all circular samples seen in Figure 2 align in a hexagonal lattice, in such a way that the visibility within one large circle can be measured. The result is shown in Figure 4, in the nine-companion configuration. Each companion element (labled A to I) produces a pair of visibility samples with all elements in the central array. The samples shown in Figure 4(mid) shows the visibility sample at one instant. By rotating the central array, the interferometer is able to sample circular areas as shown in Figure 4(bottom). For a circular visibility sample only the visibility samples within the circular effective aperture is considered.

The result of such a configuration is that the maximum baseline, i.e. the effective aperture diameter, is 3.6 times the arm length of the central Y-shaped array. This quantity is specific to the nine-element configuration, and can be scaled up, as listed in Table I.

For improved spatial resolution, the arms are made as long as possible. These arms are uniformly populated by antenna elements such that the minimum separation between the antennas satisfy the aliasing limit of the required field of view. For the Earth-disc from geostationary altitude, this is approximately 3λ.

The example tabulated in Table I uses a central satellite of equivalent size to SMOS, with 4 m arm length and equivalent satellite mass. The required number of correlators is equal to the number of baseline pairs, which in this concept increases linearly with the number of companion satellites.

The mass of microsatellites are estimated using the payload-satellite mass ratio found in [7]. The payload for each satellite is a single receiver and a Mbps communication instrument with the central satellite. At 53 GHz, the size of the antenna is small, as used in GAS [1]. From this information total payload mass of the microsatellite should be within 20 kg. Assuming payload-to-satellite mass ratio of 20% to 30%, the total mass of the microsatellite is 67 kg to 100 kg.

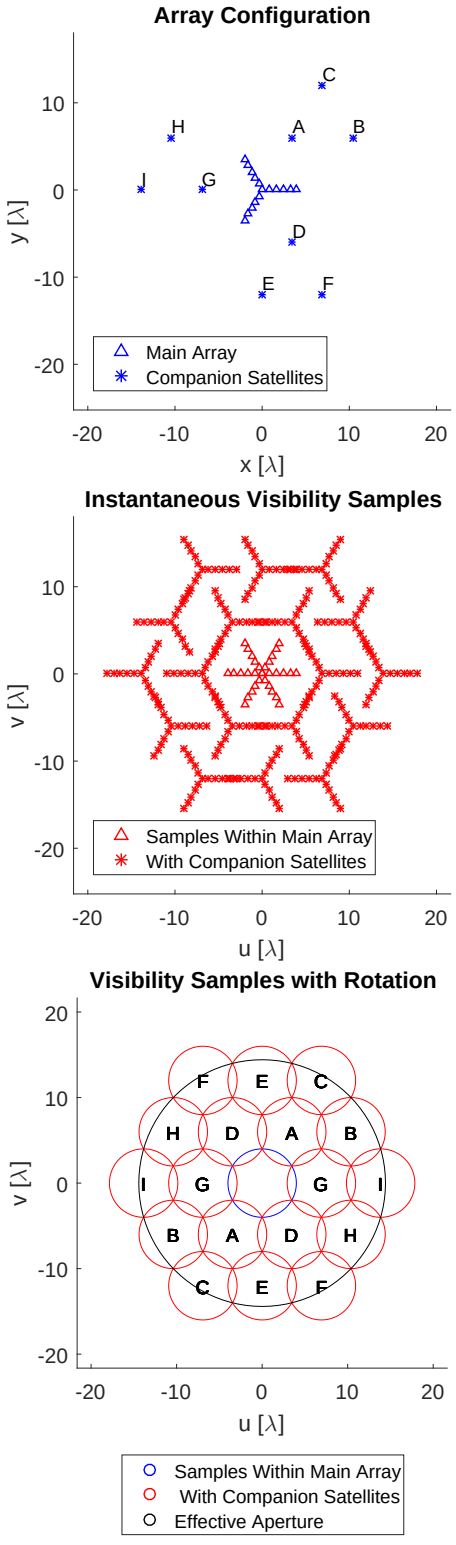

Fig. 4: A nine-microsatellite configuration of the Single-Element Companion concept with a rotating Y-shaped central array. The rotation leads to a circular effective aperture, the diameter of which is 3.6 times the length of the arms.

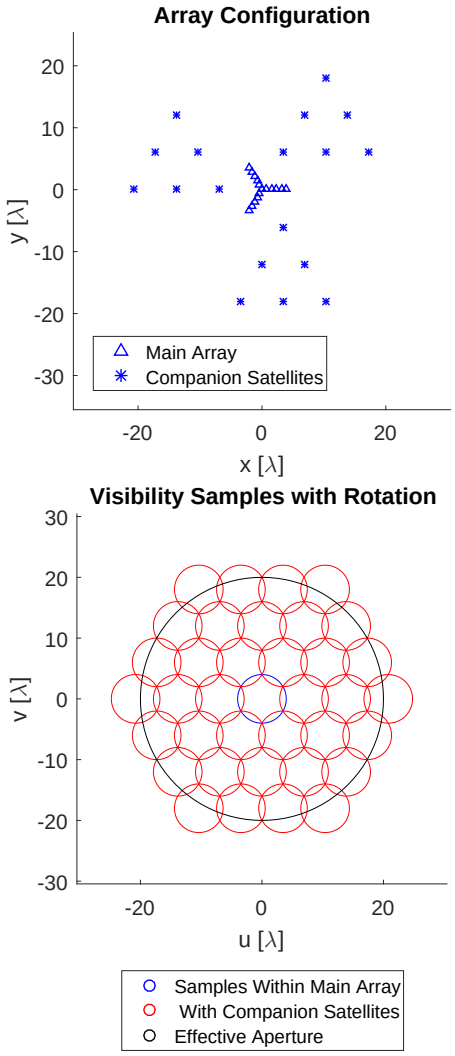

Fig. 5: An example of an up-scaled, 18-microsatellite configuration of the Single-Element Companion concept with increased effective aperture diameter of 5 times the length of the arms.

Companions	Scaling	Effective Aperture [m]	Mass [kg]
3	2.0	8.0	868
9	3.6	14.4	1288
18	5.0	20.0	1918
30	6.5	26.2	2758
45	8.0	32.0	3808
63	9.6	38.2	5068

TABLE I: The scaling and system mass of the Single-Element Companion concept shown in Figure 4. The effective aperture assumes 4 m booms on the central array.

IV. The Array Duplicate Concept

The second concept employs a constellation of six rotating two-boom interferometers flying in a triangular formation. Shown in Figure 6 is such an example. As with the first concept, the rotation of the arrays result in a hexagonally arranged visibility sample. It is notable that despite the dissimilarity of the array configurations, the resultant visibility sampling pattern is identical to the first concept. The difference can be found in the requirement that all arrays rotate simultaneously, and the effective aperture is much larger compared to the first concept for the same boom length.

Another notable difference lies in the presence of redundant baseline pairs. Shown in Figure 6, the instantaneous visibility samples A can now be sampled independently by each array, resulting in five redundant measurements. Similarly, visibility samples B are sampled between array a and b, array f and a, and array e and c, resulting in two redundant measurements, and similarly for baselines C and D. Each of E and above have no redundant measurements.

These redundant measurements represent six- and three-fold increase in available integration time, and should translate to improved array sensitivity when compared to single-measurements available in the Single-Element Companion concept. The availability of redundancies should also aid in array calibration, as well as robustness against spatial deviations resulting from free-flight. This means however that more correlators will be required than the Single-Element Companion concept, in fact the number of correlators required now increases by the square of the number of satellite.

As with the Single-Element Companion concept the triangular constellation is also scalable for larger effective apertures, as summarised in Table II. Assuming that the mass of each satellite is identical to that of SMOS, it is expected that the total constellation mass of this concept will be heavier than the first concept, potentially requiring multiple launches to fully deploy the constellation.

Satellites	Scaling	**Effective Aperture [kg]**	**Mass [kg]**
3	4.0	16.0	1974
6	7.2	28.8	3948
9	10.0	40.0	5922
12	13.1	52.5	7896
15	16.0	64.0	9870
18	19.1	76.3	11844

TABLE II: The scaling and system mass of the Array Duplicate concept shown in Figure 6. The effective aperture assumes 4 m booms on the central array.

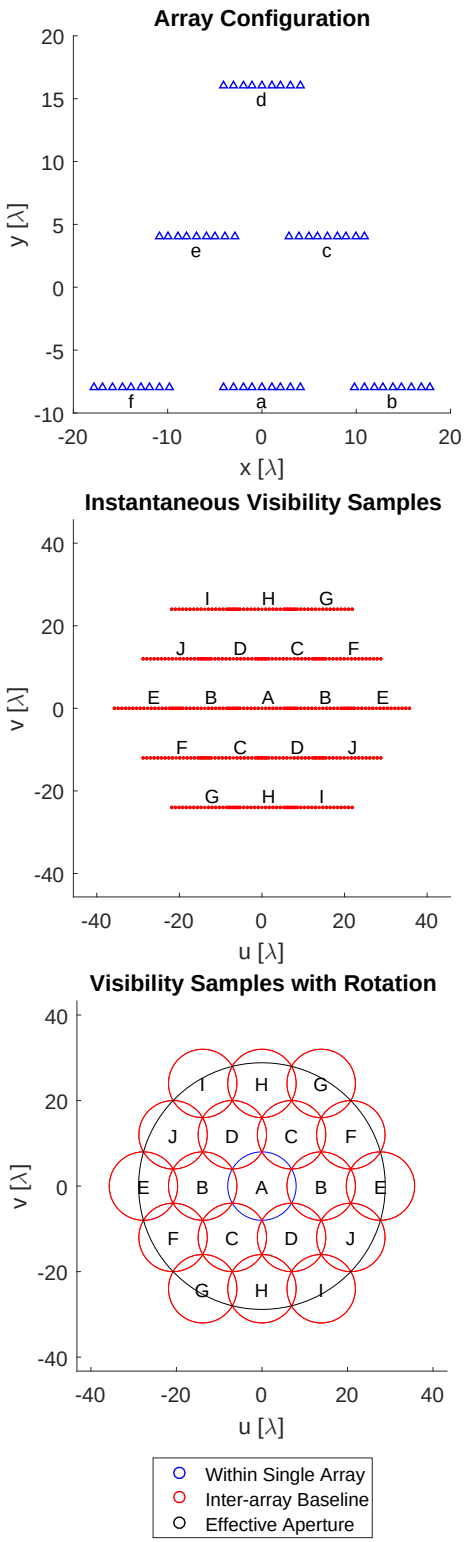

Fig. 6: An example of a six-satellite configuration of the Array Duplicate concept with rotating two-boom interferometers. All booms rotate synchronously to develop a circular aperture with diameter of 7.2 times the length of the boom.

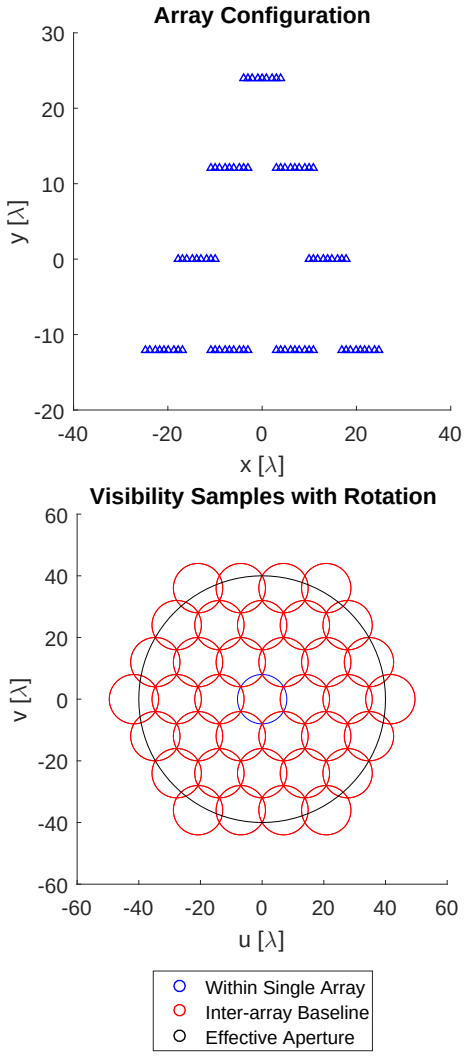

Fig. 7: An up-scaled nine-satellite configuration of the Array Duplicate concept with an effective aperture of 10 times the length of the boom.

V. Visibility Inversion Algorithm

As described in Section II, the measurement taken by the interferometer is that of the visibility of the scene. In order to recover the visibility map from this measurement, the visibility must be inverted by an inversion algorithm.

Had the visibility been measured in a regular grid, such as rectangular or hexagonal grids, the Fast inverse Fourier Transform could be used. However, since the measurement of the proposed array is taken at interlaced radial grids, the visibility samples are directly inverted, such that

$$\tilde{T}_B = \sum_{i=1}^{N} V_i W_i G_i e^{2\pi i(u_i\xi + v_i\eta + w_i\sqrt{(1-\xi^2-\eta^2)})} \quad (2)$$

For N visibility samples where V_i, u_i, v_i, w_i is the i-th visibility sample, horizontal, vertical and normal components of the baseline respectively, with generally non-zero w_i.

W_i is the windowing function applied to reduce the strength of the side-lobes and improve the efficiency of the beam, whereby improving the interferometer's sensitivity. See figure for an example of side lobes. Substantial studies have been performed in the past for finding the optimal windowing function for Earth-observation interferometry, and this is used. For this study, the Blackman window is used, defined as follows. [4]

$$W_i = 0.42 + 0.5\cos(\pi\rho_i) + 0.08\cos(2\pi\rho_i) \quad (3)$$

where $\rho_i = \sqrt{u_i^2 + v_i^2}/R_{max}$ and R_{max} is the effective aperture.

G_i is the density taper weighting function, and is equivalent in the continuous inverse Fourier transform of the differential area $\mathrm{d}u\mathrm{d}v$. Had the sampling been regular, this would be a constant value which can be accounted for after applying the inverse Fourier transform. Since the sampling is irregular, each sample has a unique differential area associated with it. This is found using the following properties of the sampling pattern.

Since the antenna placement on the arms is at constant interval and the visibility samples are taken regularly at constant angular interval, the visibility sample density is linearly decreasing from the centre of the circular sample. This means the area each visibility sample covers can be found as:

$$G_{ia} = r\delta r\delta\theta \quad (4)$$

where r is the distance to the centres of the circular visibility samples, not the origin of the visibility, δr is the radial distance between successive visibility samples, and $\delta\theta$ is the angular distance between visibility samples.

This is illustrated in Figure 8. Sampling density decreases linearly as the distance to the centre of the circular sample increases. This results in a linearly increasing weighting function, as calculated by equation 4.

Another important observation is the presence of overlapping areas, as shown in figure. Since these areas are accounted for twice, visibility samples falling within these areas are divided by two.

$$G_{ib} = \begin{cases} \frac{1}{2} & \text{in overlap zone} \\ 1 & \text{otherwise} \end{cases} \quad (5)$$

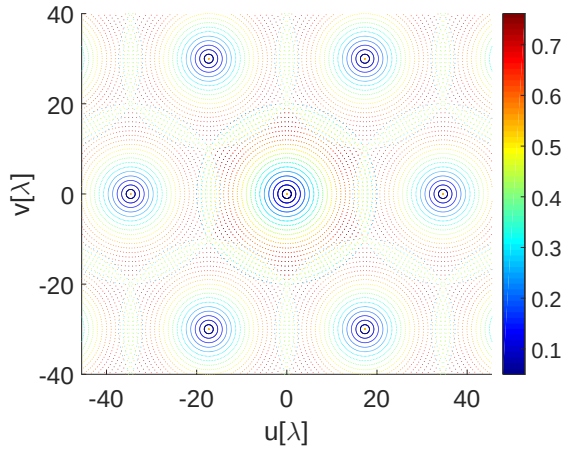

Fig. 8: The visibility sampling pattern obtained by the Single-Element Companion concept and the weighting functions associated to each point-sample. These values are calculated by equation 6. The array has 20 antenna elements per boom separated at 1 λ.

Parameter	Value
Boom Length	4 m
Minimum Baseline	2λ
Number of Antennas per Arm	67
Number of Companions	9
Maximum Baseline	14.4 m
Windowing Function	Blackman

TABLE III: Parameters of the simulated Single-Element Companion concept with nine companion satellites at 10 GHz. The beam produced by this array is shown in Figure 9.

and

$$G_i = G_{ia} G_{ib} \tag{6}$$

This is also illustrated in Figure 8, where sharp falls in the weighting function is visible in the overlapping zones.

Using the Blackman windowing function, the normalised beam pattern of the Single-Element Companion concept with nine companion satellites has been simulated at 10 GHz. The size of the array is summarised in Table III. The resultant beam patter, the array factor is shown in Figure 9, and the beam performance is shown in Table IV. The hexagonal pattern of side-lobes is attributed to the hexagonal arrangement of the circular sampling patterns, and it is generated by the discontinuities defined in equation 5 at the interfaces between the overlapping regions, as well as the zeros present in 4 at the centres of each visibility samples.

The result of using this beam to image the Earth from the geostationary orbit is shown in Figure 10. Figure 10 (top) shows the input image presented to the simulator. The image has been obtained from the GOES13, and

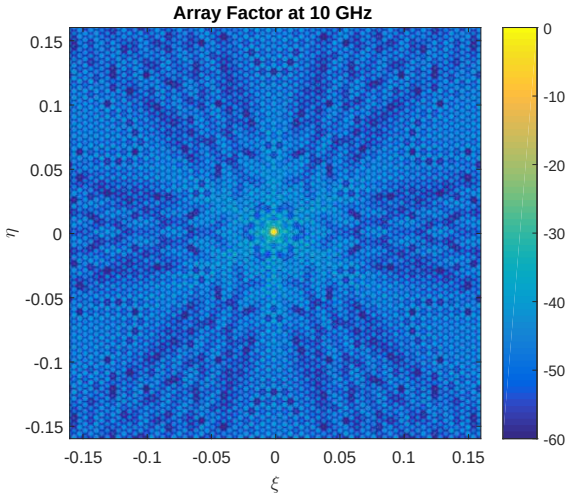

Fig. 9: Normalised beam pattern of the Single-Element Companion concept shown in Figure 4 with parameters shown in Table III from the geostationary orbit. The performance of this beam is listed in Table IV.

	Concept 1	Concept 2
-3dB Beam Efficiency	31.3%	
Null Beam Efficiency	70.0%	
-3dB Beam Width	79.5 km	39.8 km
Null Beam Width	194.1 km	97.1 km
Side-Lobe Level	-29 dB	

TABLE IV: Simulated beam performance of the Single-Element Companion concept and the Array Duplicate concept at 10 GHz from the geostationary orbit.

modified in brightness to represent the structures the interferometer may resolve. The output is shown in Figure 10 (mid), with a spatial resolution of 79.5 km at 10 GHz, and 10 (bottom) shows the difference between 10 (mid) and 10 (top) passed through the equivalent Blackman low-pass filter.

The error found in Figure 10(bottom) is large, and should be reduced by the CLEAN algorithm [6], or by reducing the minimum separation of the antennas. Indeed, by halving this separation, the error settles well under 1 K over the Earth disc, however this requires twice as many antenna elements.

Because the second concept has a very similar visibility sampling patterns, its beam performance is virtually identical to that of the Single-Element Companion concept.

VI. Effect of Array Deviation

Since the results of the visibility inversion algorithms depend on the baseline vectors, this depends on the exact relative position of the satellites. Without the correct knowledge of u, v and w, the inverted brightness map $\tilde{T}_B$ will include errors.

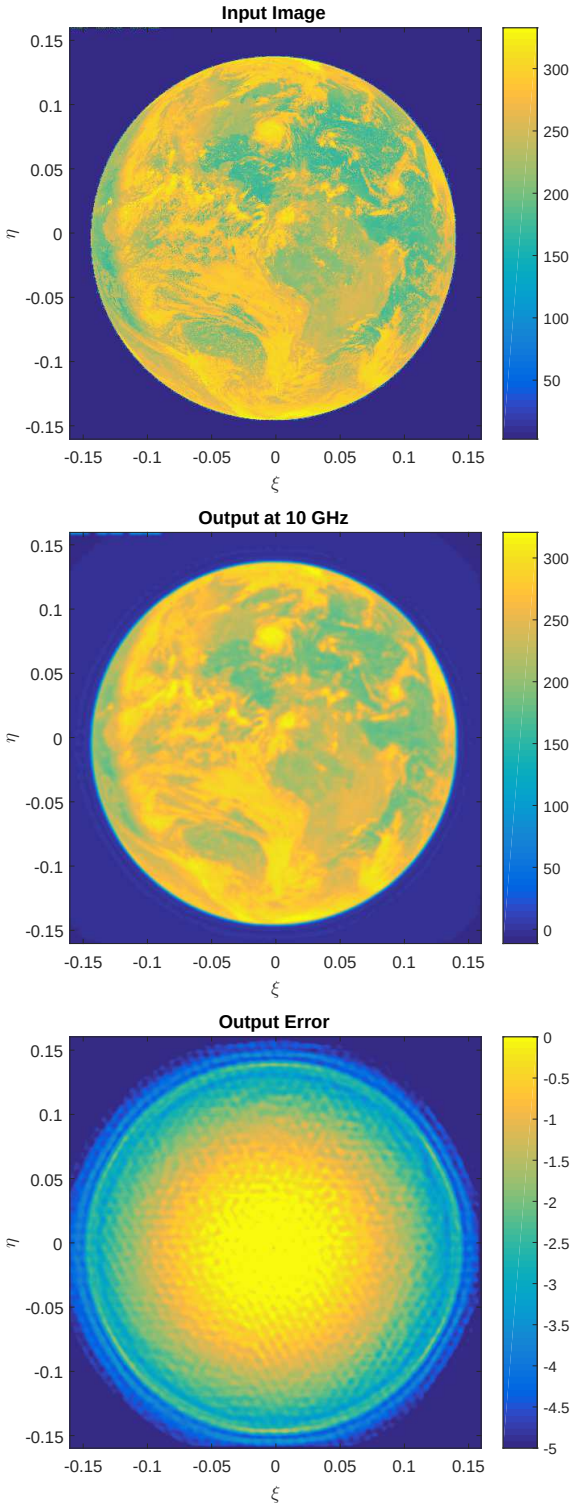

Fig. 10: Input image of the Earth from GEO (top), the reconstructed image from an array described in Table III (mid), and the difference between the input and output (bottom).

For a free-flying system such as the concepts discussed, where the satellites and the antennas on board are free to move, this effect is of major importance.

The errors arise from the fact that the physical baseline vectors (u_p, v_p, w_p) which determine the value of the visibility sample by equation 1 differs from the nominal baseline vectors (u_n, v_n, w_n), which the inversion algorithm assumes to invert the visibility samples as calculated in equation 2.

This effect has been simulated by using (u_p, v_p, w_p) to compute the visibility samples, and (u_n, v_n, w_n) to invert them and compute the resulting error in the retrieved brightness temperature map. The results of three different displacement magnitudes for the nine-companion Single-Element Companion concept and the six-satellite Array Duplicate concept are compared with their respective nominal outputs, when the deviation is zero. The three levels of deviation satellite relative position are at 0.01λ, 0.1λ and 1λ, both in-plane and 3D (in-plane and out-of-plane) deviations are shown. Figures 11 and 12 show the errors on the Single-Element Companion concept with the respective magnitude and direction of satellite relative position deviation, and Figures 13 and 14 show the corresponding results for the Array Duplicate concept.

It can be immediately seen that the out-of-plane deviation of the satellites have much larger impact than in-plane deviation in both cases, where the difference can be as high as an order of magnitude. It can also be seen that the Array Duplicate concept, thanks to higher redundancy available in their visibility sampling points, is more robust against deviations of satellite relative positions. The difference again can be as high as an order of magnitude.

The general conclusion for these simulations is that the imaging performance of the constellation is very sensitive to the uncertainties in satellite relative position measurements, where an error of a tenth of a wavelength can lead to brightness temperature errors of up to 20 K. The orbital stability of the constellation is therefore a key determinant of the array performance and of great concern to the feasibility of the arrays. This leads to the study of the orbital behaviour of such constellations on the geostationary orbit.

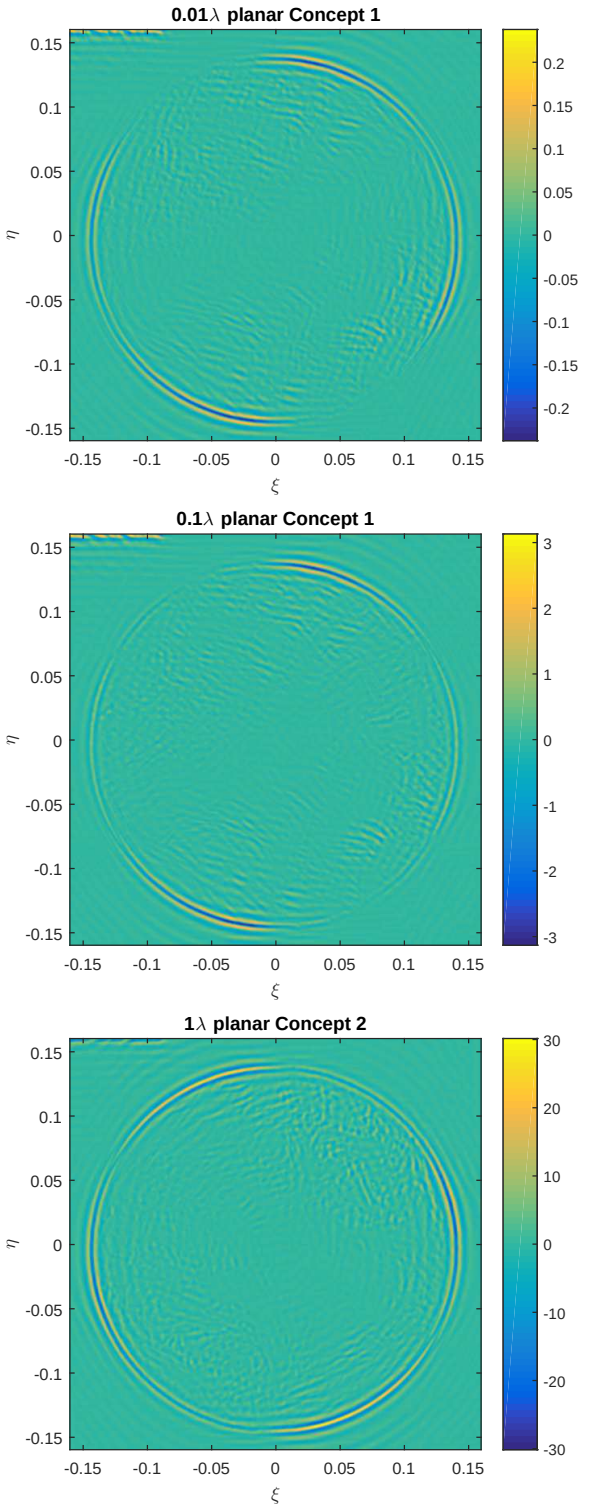

Fig. 11: Brightness temperature error resulting in Figure 10(mid) due to array deviation of the Single-Element Companion concept by 0.01λ (top), 0.1λ (mid), and 1λ (bottom) in the planar direction

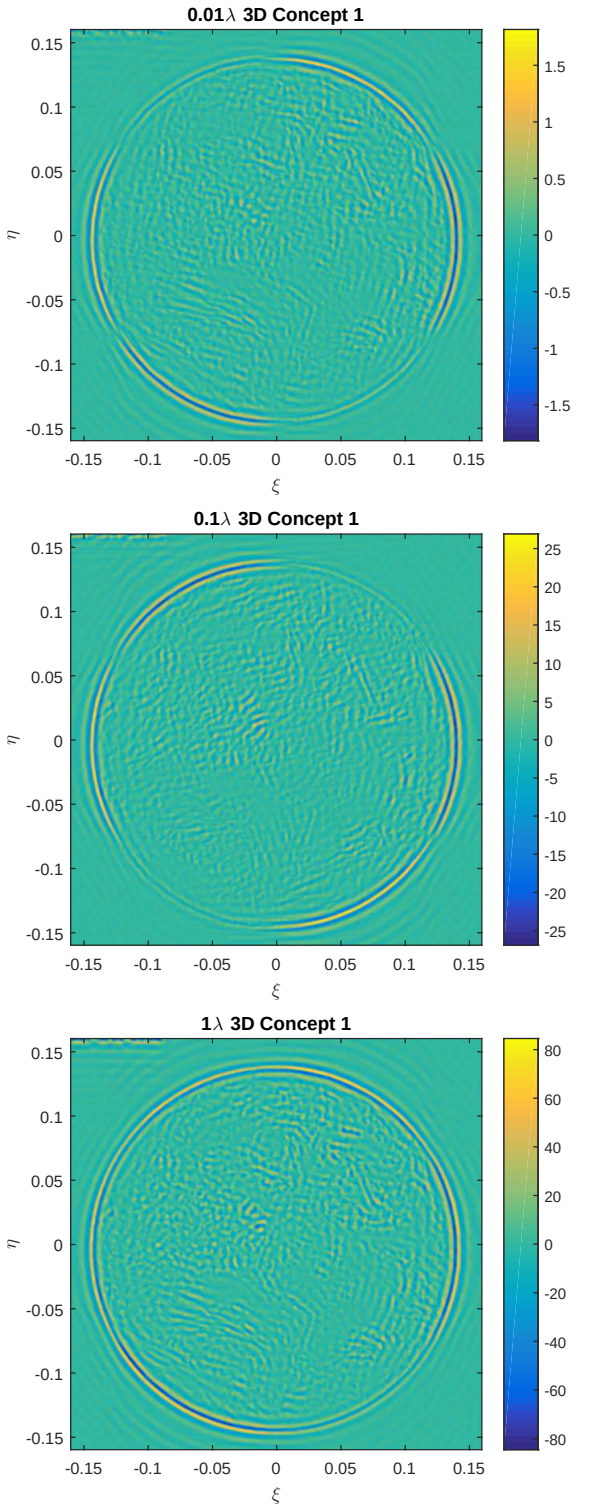

Fig. 12: Brightness temperature error resulting in Figure 10(mid) due to array deviation of the Single-Element Companion concept by 0.01λ (top), 0.1λ (mid), and 1λ (bottom) in all three directions

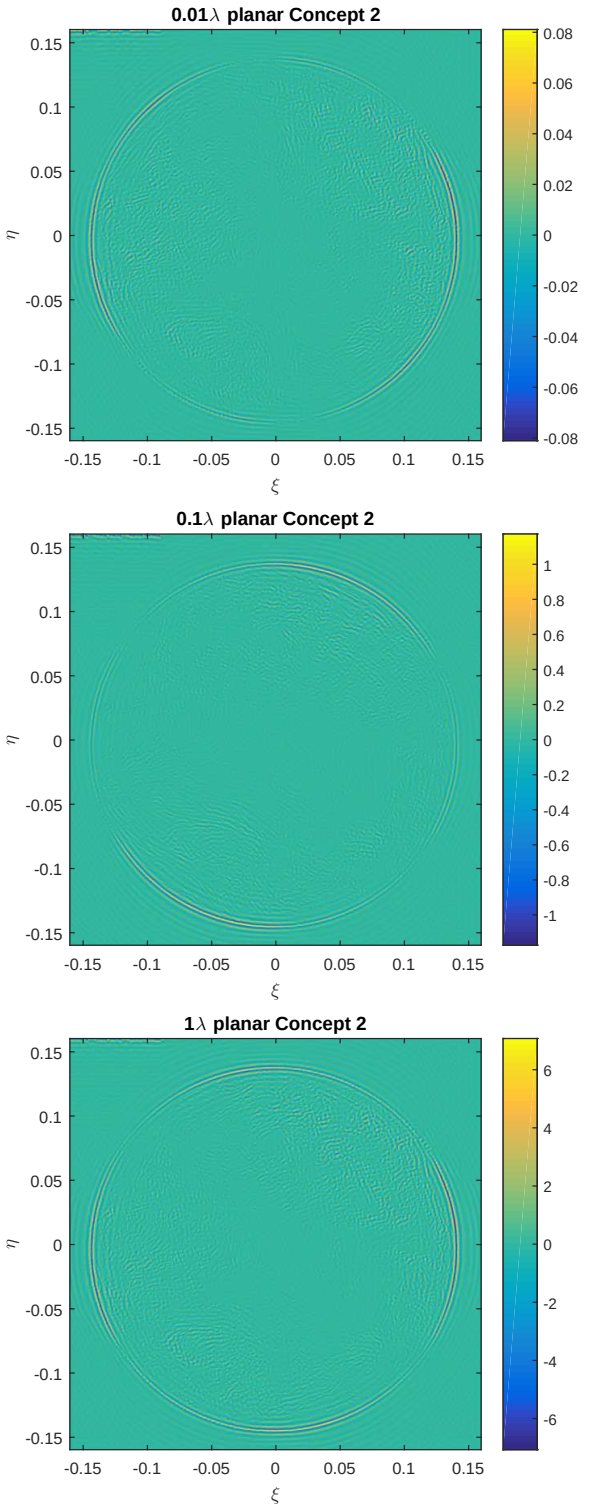

Fig. 13: Brightness temperature error resulting in Figure 10(mid) due to array deviation of the Array Duplicate concept by 0.01λ (top), 0.1λ (mid), and 1λ (bottom) in the planar direction

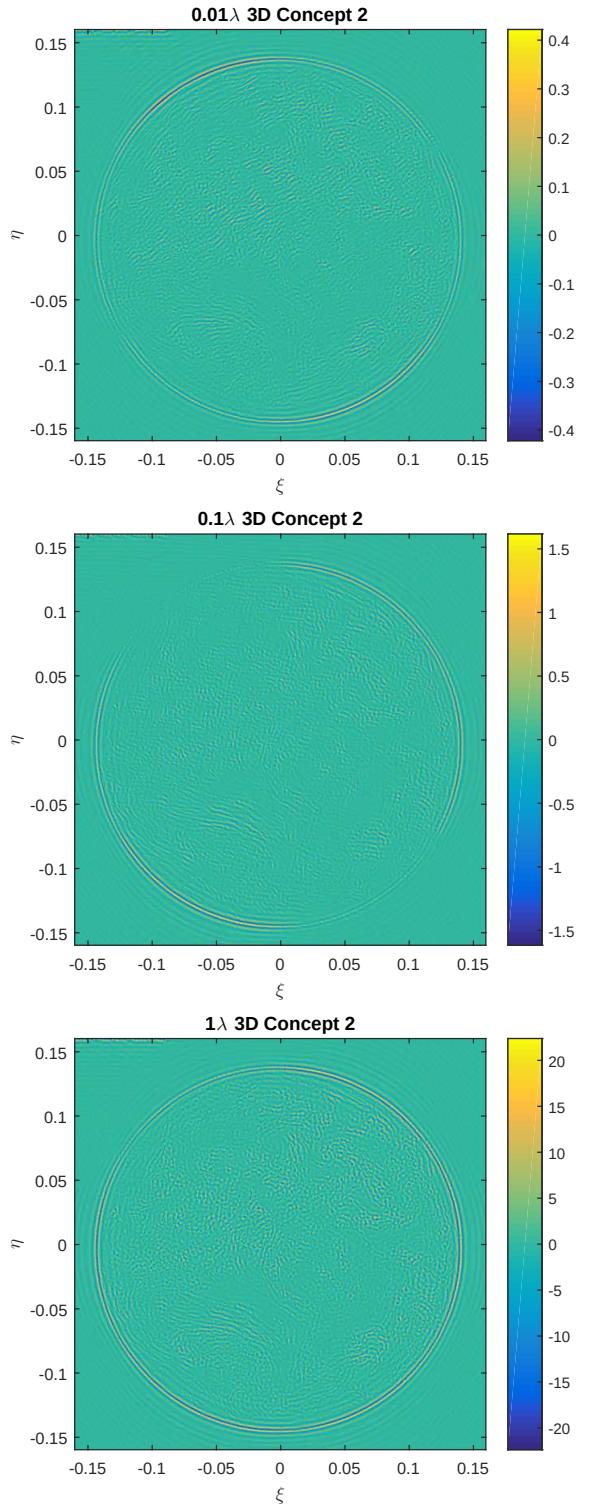

Fig. 14: Brightness temperature error resulting in Figure 10(mid) due to array deviation of the Array Duplicate concept by 0.01λ (top), 0.1λ (mid), and 1λ (bottom) in all three directions

VII. Unperturbed Orbital Behaviour of the Constellation

Naively placing the constellation on the geostationary orbit would not result in a static constellation. In fact, this will result in the tendency of all satellites to the north of the central satellite to fall to the south, and vice versa for the satellites on the south. If left uncontrolled, these satellites will undergo simple harmonic oscillation in the north-south direction, centred at the orbital plane of the central satellite.

The dynamics of such a relative motion without the presence of perturbation forces can be described by the Hill's equations of relative orbital motion. This set of equations describes the trajectory of a satellite about another satellite that is also in orbit. The trajectory is defined in a dynamic coordinate frame centred at the chief satellite, named the Hill frame, and the trajectory of the deputy satellite in this frame is defined as the relative orbit. The Hill's equations hold in a two-body problem with circular chief orbit, and when the distance between the satellites is negligible compared to the chief semimajor axis, and can be used to study the trajectory of a cluster of deputy satellites about a single deputy satellite.

It is important to note that the chief satellite can be any physical satellite that is convenient in defining the formation flight geometry, such as the central satellite in the case of Single-Element Companion concepts, or it can be a fictitious satellite that is convenient in defining the constellation, such as the centroid of the triangular formation in the case of Array Duplicate concepts.

The Hill's equations of motion are [8]

$$\ddot{x} - 2n\dot{y} - 3n^2 x = 0 \tag{7}$$

$$\ddot{y} + 2n\dot{x} = 0 \tag{8}$$

$$\ddot{z} + n^2 z = 0 \tag{9}$$

where x, y and z are displacements in R, S and W axes in the Hill frame respectively (see figure 15), and n is the chief mean orbital rate given by

$$n = 2\pi\sqrt{\frac{a_c^3}{\mu_\oplus}} \tag{10}$$

for chief semi-major axis a_c and Earth's gravitational parameter $\mu_\oplus$.

To which the solution trajectories are

$$x(t) = A_0 \cos(nt + \alpha) + x_{off} \tag{11}$$

$$y(t) = -2_0 \sin(nt + \alpha) - \frac{3}{2} n t x_{off} + y_{off} \tag{12}$$

$$z(t) = B_0 \cos(nt + \beta) \tag{13}$$

for amplitude parameters A_0 and B_0, phase parameters α and β, and initial offsets x_{off} and y_{off}. Note that for a bound orbit, x_{off} must be zero.

Using the Hill's equation 9, it can be found that the continuous acceleration required for the deputy satellites to prevent itself from falling into the chief satellite is approximately 5.3×10^{-9} ms^{-2} per metre of displacement from the chief orbital plane. This force allows the deputy satellite to levitate off the chief orbital plane.

Continuous thrust required to achieve this acceleration should be in the order of 0.37 μN and 3.5 μN per metre of levitation for the Single-Element Companion case and Array Duplicates respectively.

Furthermore, this requirement presents complications in designing thruster configuration, as it requires the thrust vectors to be pointing directly to other satellites within the constellation.

An alternative to this approach is the use of a suitable relative orbit, described by equations 11 through 13. Indeed, a set of convenient solutions exist which allows the deputy satellites to oscillate north and south, while maintaining the constellation facing (generally) toward the Earth. The key is to allow the north-south oscillation by introducing a synchronous east-west oscillation. This is done by the introduction of differential eccentricity, which, unfortunately also introduces out-of-plane oscillation of the constellation.

This is shown in Figure 15. The radial direction in the Hill frame is the Earth-chief satellite vector, which places the Earth in the -x axis of this frame. The z-axis points toward the chief orbit normal. Shown in red are the instantaneous positions of the satellites of the configuration shown in Figure 5, and shown in blue are the relative orbital trajectories of each of these satellites. The orbital period of these relative orbit equals the chief orbital period, allowing all deputy satellites to complete their orbits in equal time. This leads to a rigid-body-like rotation in the z-y directions while also oscillating in the radial direction.

The performance of this option can now be compared to the option where the relative orbit is fixed by means of continuous thrust. To achieve the sub-mm precision required for the application, the relative orbits are propagated including the dominant perturbation forces found in the geostationary orbit.

VIII. Propagation of Relative Orbits

Although the Hill's equations describe the general motion of a formation flight, it requires the chief orbit to be exactly circular - an assumption never exactly true even for a geostationary orbit- and they do not account for perturbation forces present in the geostationary orbit.

To account for these effects, Newton's equations of motion has been numerically propagated. The equation

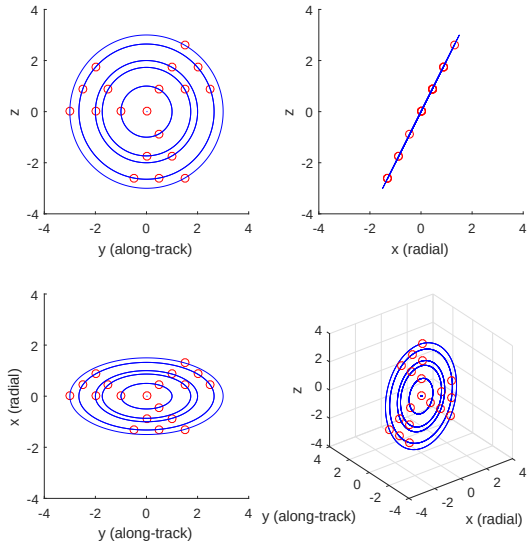

Fig. 15: Relative orbits suitable to the interferometry application, found by Hilld equations 11 to 13. Instantaneous satellite positions of the configuration shown in Figure 5 (red), with suitable relative orbit in Hill frame (blue). Period of all these orbits is one day leading to a rotation of the constellation in the z-y axes.

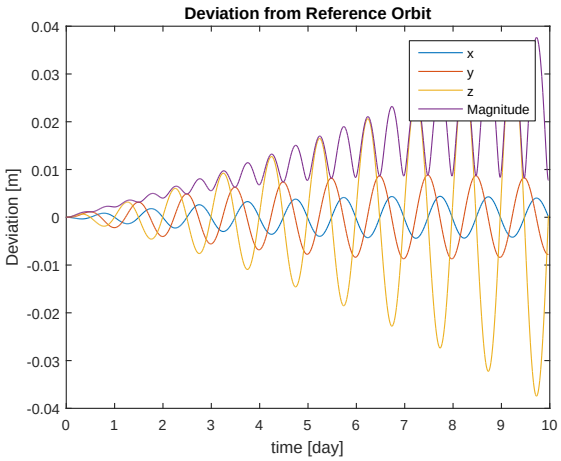

Fig. 16: Relative orbit deviation due to aspherical gravitational field (up to $C_{5,5}$)

of motion takes into account the three dominant perturbation forces listed below, as well as the Earth's gravitational attraction.

a) Earth's aspherical gravitational field: The Earth's gravitational potential is not exactly spherical, and can be better approximated by the spherical harmonics model. In this study the EGM-08 model is used, also found in [5]

b) Multi-body perturbations of the sun and the moon: The gravitational forces exerted by the sun and the moon have affect the orbit of chief and deputy satellites differently, thus having an effect on the relative orbit. This effect is propagated using an ephemeris to locate the sun and the moon [10]

c) Solar radiation pressure: The magnitude of the radiation pressure will be different for the chief and deputy satellites, if the product of their area-to-mass ratios and surface reflectivities are different. The cannonball model of SRP is used, while the location of the sun is found from an ephemeris [10].

The chief and deputy orbits are propagated independently, then their relative motion is transformed into the Hill frame. To ensure that the integration steps are sufficiently small to provide the necessary precision, steps have been chosen such that when propagating a two-body problem, the propagated orbit converges toward a Keplerian orbit in sub-mm accuracy. Below are brief descriptions of the perturbation forces considered.

Uncontrolled, the strength of differential solar radiation pressure dominates the relative dynamics of the constellation. Shown in Figures 16 through 20 Are the deviations in a 10-m radius relative orbit as shown in Figure 15 due to the dominant perturbation forces in the geostationary orbit.

Figure 17 and 18 show the importance of minimising the relative perturbation forces, in order to maintain the relative orbit. While the difference in the area-to-mass ratio of the central satellite and the companion satellites amount to large differential solar radiation perturbation, under the assumption that all duplicate arrays are equal in size and mass, the differential solar radiation perturbation is small. Perturbations due to the third body forces are of comparable magnitude, however as the differential force they impose on the chief and deputy satellites are negligible, their effects on the relative orbit are small compared to the differential solar radiation pressure.

IX. Station-Keeping Strategies

The application finds that the collective position of the constellation in the geostationary orbit does not affect its radiometric performance. Rather, it is the geometry of the formation-flight which is the key performance driver. Herein, the station-keeping strategy for the mission are separated into two distinct strategies which can be executed independently. The first strategy is to control deputy satellites to maintain their reference relative orbit about a non-cooperative chief satellite. This is achieved by counteracting the differential perturbation forces, defined as the difference in perturbation experienced by the chief satellite and the deputy satellite. This is the force that perturbs a relative orbit. The second strategy is to maintain the collective station of the constellation

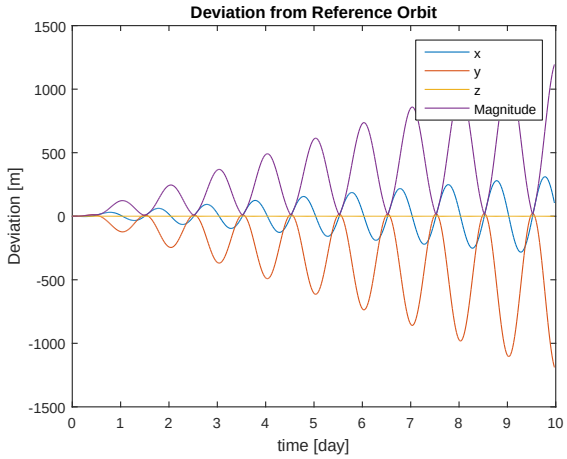

Fig. 17: Relative orbit deviation due to solar radiation pressure (Single-Element Companions)

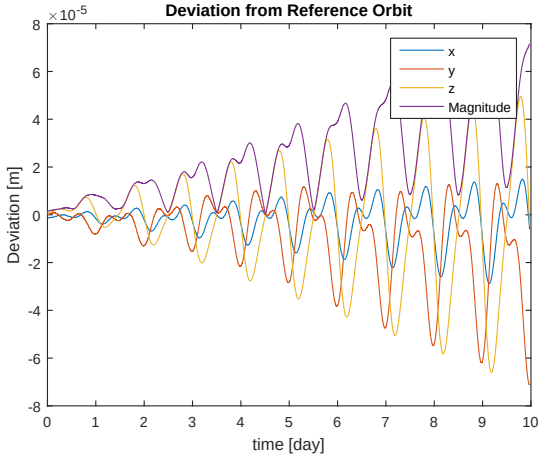

Fig. 18: Relative orbit deviation due to solar radiation pressure(Array Duplicates)

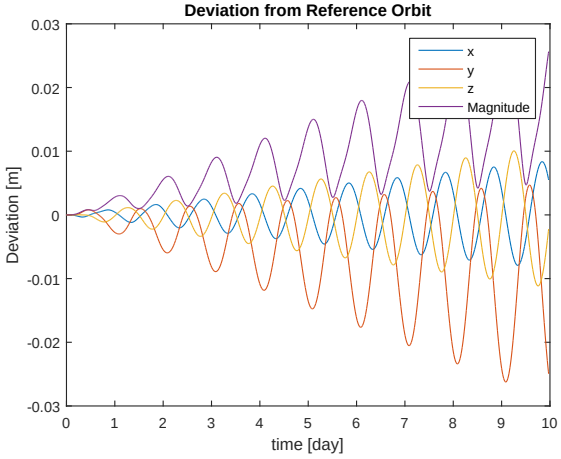

Fig. 19: Relative orbit deviation due third-body forces (Sun)

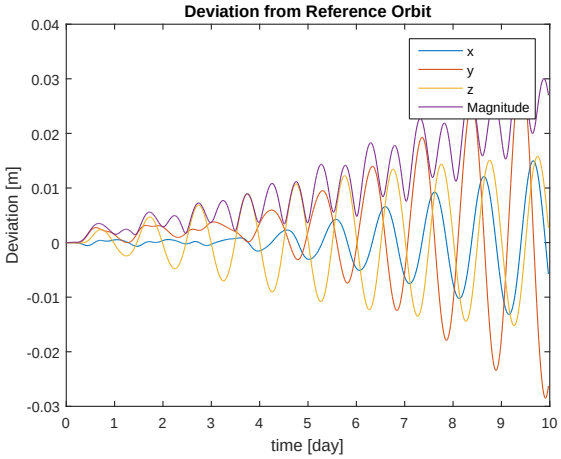

Fig. 20: Relative orbit deviation due third-body forces (Moon)

within the mission's mean orbit, which is a geostationary orbit, according to the regulations for the orbit. This is achieved by counteracting the perturbation forces, and the standard station-keeping strategies developed for geostationary satellites are directly applicable.

Summarised in Table V are the formation-keeping ΔV requirements for first mission concept implemented in the two formation options discussed. Table VI summarises the requirements for the second mission concept.

	Single-Element Companion Concept	
	Relative Orbit	**Fixed**
$\mathbf{C}_{5,5}$	4.10×10^{-4} m/s	1.32×10^{-4} m/s
SRP	5.53×10^{-1} m/s	5.53×10^{-1} m/s
MBP (Sun)	3.34×10^{-4} m/s	5.27×10^{-5} m/s
MBP (Moon)	3.62×10^{-4} m/s	1.66×10^{-4} m/s
Levitation	0 m/s	1.67×10^{0} m/s
Total	5.54×10^{-1} m/s	2.23×10^{0} m/s

TABLE V: Contributions of differential perturbation acceleration sources to the annual formation-keeping ΔV requirements for 10 m relative orbit, for the Single-Element Companion mission concept.

	Array Duplicate Concept	
	Relative Orbit	**Fixed**
$\mathbf{C}_{5,5}$	4.10×10^{-4} m/s	1.32×10^{-4} m/s
SRP	2.69×10^{-4} m/s	8.11×10^{-7} m/s
MBP (Sun)	3.34×10^{-4} m/s	5.27×10^{-5} m/s
MBP (Moon)	3.62×10^{-4} m/s	1.66×10^{-4} m/s
Levitation	0 m/s	1.67×10^{0} m/s
Total	1.38×10^{-3} m/s	1.67×10^{0} m/s

TABLE VI: Contributions of differential perturbation acceleration sources to the annual formation-keeping ΔV requirements for 10 m relative orbit, for the Array Duplicate mission concept.

X. Conclusion

By exploring the effects of performing interferometry between multiple free-flying arrays, two viable mission concepts for microwave interferometry have been presented. The first concept is a Single-Element Companion concept with a rotating Y-shaped interferometer flying in close formation with several formation-flying microsatellites. Apertures larger than 14.4 m can be synthesised, which can be scaled larger by increasing the number of accompanying microsatellites. The second concept is the Array Duplicate concept, with six or more rotating two-boom interferometers flying in a triangular formation. Apertures of 28.8 m and larger can be synthesised, similarly, by increasing the number of formation-flying satellites.

It has been found that while the Array Duplicate concept is capable of synthesising larger apertures, the Single-Element Companion option has the advantage of being deployable in a single launch. The length of the maximum baseline achievable per unit mass of the constellation however are roughly equivalent.

Such large synthetic apertures are unprecedented for Earth observation, and may be applied to unprecedented spatial resolution, or a radiometry mission to the geostationary orbit.

While the direct inverse discrete transform method used is found to achieve main beam efficiencies of 70% from the geostationary orbit, other inversion algorithms may be applied to approach the limit set by the Blackman window, at 99%.

The arrays have been found to be highly sensitive to errors in satellite relative position measurement, where errors as small as a tenth of the wavelength can result in up to 20K error in the retrieved brightness temperature.

By direct propagation of Newton's equations motion, accounting for solar radiation pressure, third body forces and the Earth's aspherical gravitational field, the formation-keeping fuel required to maintain the nominal relative orbit is found at up to 2.23 m/s annually.

XI. Acknowledgements

This research has been funded by the UK Engineering and Physical Sciences Research Council (EPSRC). Award Reference number 1503202

Participation to the IAC2016 has been funded by Japan Aerospace Exploration Agency (JAXA).

References

[1] Tanner, A. B.; Wilson, W. J.; Lambrigsten, B. H.; Dinardo, S.; Brown, S.; Kangaslahti, P.; Gaier, T.; Ruf, C.; Gross, S.; Lim, B.; Musko, S.; Rogacki S.; Piepmeier, J., "Initial Results of the Geostationary Synthetic Thinned Array Radiometer (GeoSTAR) Demonstrator Instrument," *IEEE TRANSACTIONS ON GEOSCIENCE AND REMOTE SENSING,* 2007.

[2] Christensen, J.; Carlström, A.; Ekstrom, H.; Emrich, A.; Embretsén, J.; de Maagt, P.; Colliander, A., "GAS: the Geostationary Atmospheric Sounder," in *Geoscience and Remote Sensing Symposium, 2007. IGARSS 2007.* IEEE International , vol., no., pp.223-226, 23-28 July 2007

[3] Hao Liu; Ji Wu; Shengwei Zhang; Jingye Yan; Lijie Niu; Cheng Zhang; Weiying Sun; Huiling Li; Bin Li, "The Geostationary Interferometric Microwave Sounder (GIMS): Instrument overview and recent progress," in *Geoscience and Remote Sensing Symposium (IGARSS), 2011* IEEE International , vol., no., pp.3629-3632, 24-29 July 2011

[4] Corbella, I.; Martin-Neira, M.; Oliva, R.; Torres, F.; Duffo, N., "Reduction of Secondary Lobes in Aperture Synthesis Radiometry," in *Geoscience and Remote Sensing Letters, IEEE*, vol.9, no.5, pp.977-979, Sept. 2012

[5] David Vallado. *Fundamentals of Astrodynamics and Applications*. Microcosm Press, fourth edition, 2013.

[6] A. Camps, J. Bara, F. Torres, and I. Corbella. Extension of the clean technique to the microwave imaging of continuous thermal sources by means of aperture synthesis radiometers, 1998.

[7] James Wertz and Wiley Larson. Space Mission Analysis and Design. Microcosm Press, Hawthorne,CA, 2 edition, 1992.

[8] Kyle Alfriend, Srinivas Vadali, Pini Gurfil, Jonathan How, and Louis Breger. *Spacecraft Formation Flying: Dynamics, Control and Navigation*. Elsevier, 2010.

[9] I. Corbella, N. Duffo, M. Vall-llossera, A. Camps and F. Torres, "The visibility function in interferometric aperture synthesis radiometry," in *IEEE Transactions on Geoscience and Remote Sensing*, vol. 42, no. 8, pp. 1677-1682, Aug. 2004. doi: 10.1109/TGRS.2004.830641

[10] C. Colombo, "Planetary Orbital Dynamics (PlanODyn) suite for long term propagation in perturbed environment", *6th International Conference on Astrodynamics Tools and Techniques (ICATT)*, 14-17 Mar. 2016, Darmstadt